Slip-mediated dewetting of polymer microdroplets

Joshua D. McGraw[a,b,1], Tak Shing Chan[c,d], Simon Maurer[a], Thomas Salez[e], Michael Benzaquen[e,2], Elie Raphaël[e], Martin Brinkmann[c,d], and Karin Jacobs[a,f]

[a]Soft Matter Physics Group, Experimental Physics, Saarland University, 66041 Saarbrücken, Germany; [b]Département de Physique, Ecole Normale Supérieure/Paris Sciences et Lettres (PSL) Research University, CNRS, 75005 Paris, France; [c]Fluid Interfaces Group, Experimental Physics, Saarland University, 66041 Saarbrücken, Germany; [d]Department of Complex Fluids, Max Planck Institute for Dynamics and Self-Organization, 37077 Göttingen, Germany; [e]Laboratoire de Physico-Chimie Théorique, UMR Gulliver 7083, Ecole Supérieure de Physique et de Chimie Industrielles ParisTech/PSL Research University, 75005 Paris, France; and [f]Leibniz-Institute for New Materials, 66123 Saarbrücken, Germany

Edited by Michael P. Brenner, Harvard University, Cambridge, MA, and accepted by the Editorial Board December 9, 2015 (received for review July 10, 2015)

Classical hydrodynamic models predict that infinite work is required to move a three-phase contact line, defined here as the line where a liquid/vapor interface intersects a solid surface. Assuming a slip boundary condition, in which the liquid slides against the solid, such an unphysical prediction is avoided. In this article, we present the results of experiments in which a contact line moves and where slip is a dominating and controllable factor. Spherical cap-shaped polystyrene microdroplets, with nonequilibrium contact angle, are placed on solid self-assembled monolayer coatings from which they dewet. The relaxation is monitored using in situ atomic force microscopy. We find that slip has a strong influence on the droplet evolutions, both on the transient nonspherical shapes and contact line dynamics. The observations are in agreement with scaling analysis and boundary element numerical integration of the governing Stokes equations, including a Navier slip boundary condition.

slip | contact line motion | free-surface flows | microflows | nanoflows

Unexpected flow phenomena emerge when the size of a liquid system is reduced below a length scale typically on the order of a few, to hundreds of nanometers (1–3). Approaching this scale, effects associated with interfaces become increasingly important. One such effect is slip, wherein fluid slides along a solid boundary. Flow of single-component (4, 5) and complex fluids (6, 7) in micro- and nanochannels, as well as dewetting (8, 9) and interfacial instabilities (10) of molten polymer films, are systems and phenomena in which slip may have an effect. The present work demonstrates that the relaxation of micrometer-sized droplets in contact with a solid planar surface is strongly influenced by slip. The observed dewetting dynamics exhibits an unexpectedly rich phenomenology of transient droplet shapes.

The empirical no-slip boundary condition assumes no relative motion between liquid and solid at the phase boundary. This condition was historically assumed to be valid in all practical cases (3). However, Huh and Scriven discovered (11) that the no-slip boundary condition leads to infinite viscous dissipation at the tip of a liquid wedge, and thus implies that a contact line would never move—infinite force is required to overcome infinite dissipation. In common experience we are surrounded by liquid/vapor interfaces moving along solid surfaces, from water droplets on a wind screen, to the displacement of air by liquid through a capillary or porous medium. This apparent paradox of contact line motion has attracted the attention of many researchers over at least the last four decades (11–18).

Various mechanisms have been proposed to explain the existence of contact line motion. Precursor film models (13, 19–25) circumvent the Huh–Scriven paradox as they neglect the existence of a proper contact line. Models beyond a continuum hydrodynamic description include molecular transport mechanisms at the contact line (15, 26, 27). Another commonly used approach to avoid the paradox is to allow for a slip boundary condition at the substrate (11, 12, 18, 28–31). Importantly, all of these models used in previous studies (27, 32, 33) have in common a characteristic length scale, for example the extension of the slipping region (18, 30) or the molecular hopping length (15, 27). This length scale is typically of nanometric size yet much smaller than the lateral extension of the interface, which could be that of a millimetric droplet or meniscus. For this wide separation of length scales, being at least five orders of magnitude, the deformation of the interface by viscous stresses is noticed only in the direct vicinity of a moving contact line. On a macroscopic scale, the liquid interface remains close to a quasi-static shape (17, 34, 35). Millimetric sessile drops relaxing on a plane surface, for instance, are described by a sequence of spherical caps with a slowly changing apparent contact angle. In such a multiscale system, the microscopic length has only a weak (logarithmic) effect on the dynamics (13, 16).

Recently, the no-slip hypothesis has been critically assessed. Experimental techniques (1–3) to measure slip lengths b—defined as the distance beyond the solid over which a linear extrapolation of the liquid velocity field reaches zero (36)—have reached nanometric resolution. Values of b for small-molecule liquids on the order of tens (1–3, 37–40) up to a couple of hundred nanometers (41–43) are now reported. Polymer melts, containing chain-like molecules which can be highly coupled to one another (13, 44, 45), may show slip lengths from one up to tens of micrometers (9, 10, 46–51). The microscopic mechanisms responsible for such large slip lengths are not clear in all cases (52), e.g., for unentangled polymers dewetting from chemically similar substrates as used here (51). Whereas investigations into the molecular origin of these disparate and relatively large slip lengths continue, these self-assembled monolayers (SAMs) provide an ideal set of surfaces to study the impact of slip

Significance

Contact lines form at phase boundary intersections, quintessentially liquid/vapor interfaces at solid surfaces. Whereas classical hydrodynamic models predict that contact line motion requires infinite energy, common observations of moving droplets show that huge amounts of energy are unnecessary. Slip, wherein a fluid slides along a solid boundary, offers relief of such divergences, and has gained attention with the developing fields of micro- and nanofluidics. This article focuses on contact line motion of retracting liquid droplets with micrometric dimensions. Slip is tuned by changing a nanometric substrate surface layer. The resulting contact line motion and droplet evolutions are hugely influenced by slip, thus offering insights on the question: How do contact lines move?

Author contributions: J.D.M., T.S.C., T.S., E.R., M. Brinkmann, and K.J. designed research; J.D.M., T.S.C., S.M., T.S., M. Benzaquen, and M. Brinkmann performed research; J.D.M., T.S.C., S.M., T.S., and M. Brinkmann analyzed data; and J.D.M., T.S.C., T.S., M. Benzaquen, E.R., M. Brinkmann, and K.J. wrote the paper.

The authors declare no conflict of interest.

This article is a PNAS Direct Submission. M.P.B. is a guest editor invited by the Editorial Board.

[1]To whom correspondence should be addressed. Email: joshua.mcgraw@phys.ens.fr.

[2]Present address: Capital Fund Management, 75007 Paris, France.

This article contains supporting information online at www.pnas.org/lookup/suppl/doi:10.1073/pnas.1513565113/-/DCSupplemental.

on small-scale interfacial flows. In contrast to systems with a wide separation of length scales, a qualitatively different interfacial dynamics may be found when system sizes become comparable to the slip length.

To explore the effect of slip on small-scale wetting flows, here we study polymer microdroplets dewetting from SAMs. The slip lengths involved are comparable to the typical droplet heights. Strikingly, we find that slip significantly influences the transient droplet profiles, which are nonspherical and thus not quasi-static (Fig. 1*A*). Velocities of the receding contact lines are orders of magnitude faster than expected for no-slip systems. The good agreement between the experimental results and hydrodynamic modeling, including a Navier slip boundary condition, shows that slip is the dominating factor in the shape evolution and contact line motion of the small dewetting droplets in our experiments. Any other processes occurring at the contact line play a minor role.

The experiments were performed using spherical cap-shaped polystyrene (PS) microdroplets as the initial state, with flows driven by unbalanced capillary forces. Because of the high viscosity of the nonvolatile PS melt, droplets with a typical diameter of 1 μm reach their new equilibrium conformation on the order of several minutes to hours, and can thus be monitored with high spatial resolution using atomic force microscopy (AFM). Prepared in the glassy state with a low contact angle of $\theta_0 = 9 \pm 3°$ (24), the droplets are transferred onto Si wafers precoated with SAMs of octadecyl- or dodecyltrichlorosilane (OTS and DTS, respectively). In the liquid state, the PS/air interfaces on these two chemically similar SAMs exhibit the same equilibrium contact angles, $\theta_\infty = 62 \pm 3°$. Despite the high similarity of OTS and DTS, the slip lengths of the PS melt on these SAMs are strikingly different: $b_{\mathrm{OTS}} = 160 \pm 30$ nm and $b_{\mathrm{DTS}} = 1{,}500 \pm 200$ nm are reported in ref. 51. These slip lengths were extracted from the rim shape and velocity of a dewetting PS layer with an initially constant thickness (50, 53). See *Materials and Methods* for further details on sample preparation and experimentation.

When heated above the glass transition temperature, we observe the contact line to move inward, while volume conservation ensures that material is collected toward the center of the droplet. Fig. 1 *B* and *C* shows full sequences of axisymmetric droplet profiles, $h(r,t)$ with r and t the radial coordinate and time, respectively, observed during the dewetting process on OTS- and DTS-covered substrates. The shapes highlighted in Fig. 1*A* were chosen such that the transient profiles deviate maximally from a spherical cap, as demonstrated in Fig. 1 *B* and *C*, *Insets* (gray lines).

The PS droplet dewetting from OTS in Fig. 1*B* transiently forms a ridge and for some time exhibits a positive (inward) curvature at the droplet center. This qualitative feature was observed previously using numerical integration of a 2D thin-film equation including a precursor film (22). Additionally, the central droplet height does not change significantly until the width of the ridge is comparable to the time-dependent contact line radius, $R(t)$ (Fig. S1). In contrast to the evolution on OTS, the PS droplet dewetting from DTS does not show a pronounced ridge. Furthermore, at the earliest accessible experimental time (several minutes), the central droplet height is already increasing on DTS as seen in Fig. S1. At late times, for both OTS and DTS, the curvature is always negative (outward) as the droplets relax to their final spherical cap shapes with the same contact angle θ_∞. In addition to the equilibrium contact angle θ_∞, surface tension γ and viscosity η being identical for the PS droplets on OTS and DTS in Fig. 1, the initial contact line radii $R_0 = R(0)$ and initial contact angle were similar. The slip lengths, b, however, differ by an order of magnitude on these two substrates. The qualitative differences in the evolution are therefore expected to originate from the different values of the dimensionless slip length $\mathcal{B} = b/R_0$, as can be seen for a similar shape transition in dewetting polymer films with slip (9, 49). Indeed, a gradual disappearance of the ridge at any point in the temporal evolutions can be observed by increasing $\mathcal{B}$ for PS on OTS—decreasing R_0 in this case, with identical $b, \theta_0, \theta_\infty$, a ridge can no longer be detected for $R_0 \lesssim 2.7$ μm (Fig. S2).

To investigate theoretically whether slip is the dominating factor that controls the dewetting of PS droplets, we numerically integrated the governing fluid mechanical equations. Inertial effects are neglected because the Reynolds number $\mathrm{Re} = \rho \dot{R} R/\eta \approx 10^{-19}$, involving the mass density ρ and contact line velocity $\dot{R} = dR/dt$, is much less than unity. The flow is controlled by a balance of viscous and capillary stresses only. Solutions to the governing Stokes equation, $\nabla p = \eta \nabla^2 \boldsymbol{u}$, and incompressibility condition $\nabla \cdot \boldsymbol{u} = 0$ are numerically computed using a boundary element method (54). Here, p is the scalar pressure field and $\boldsymbol{u}$ is the velocity field. The normal stress component at the curved PS/air interface is balanced by surface tension according to Laplace's law, which reads $2\eta \partial_n u_n - p = 2\gamma \mathcal{C}$, where $\mathcal{C}$ is the mean curvature of the liquid/vapor interface, and where ∂_n denotes the directional derivative normal to this interface. Hydrostatic contributions to the pressure, elasticity of

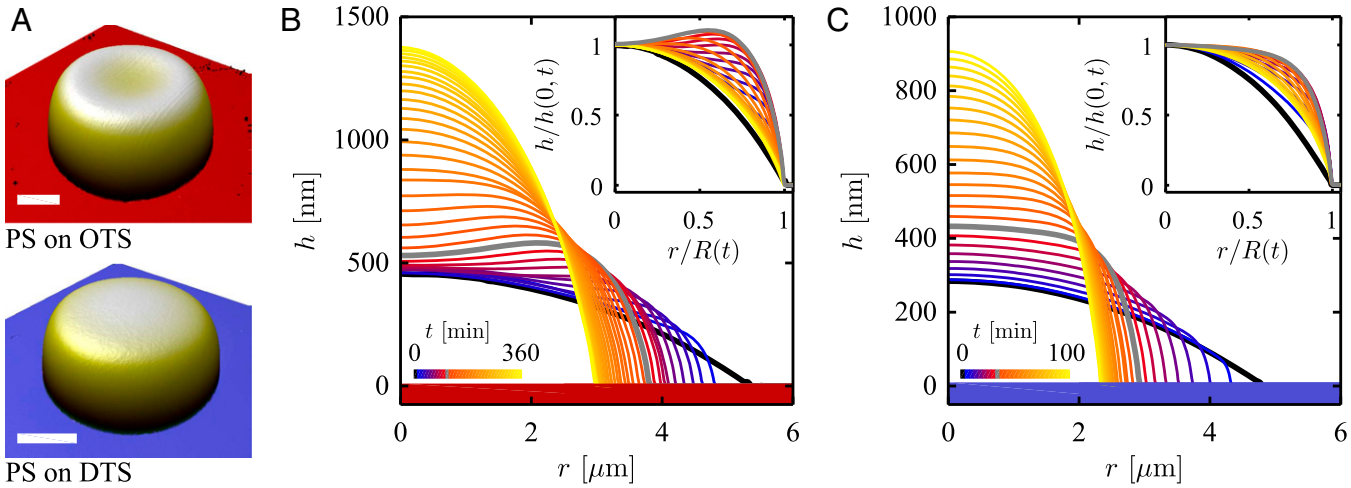

Fig. 1. (*A*) Experimental AFM data for 10.3-kg/mol PS microdroplets dewetting from OTS (*Top*) and DTS (*Bottom*) SAMs. (Scale bars: horizontal, 2 μm; vertical scale according to gray lines in *B* and *C*.) (*B*) Experimental height profile evolution of the PS droplet dewetting from OTS shown in *A*. Time between subsequent lines is ~10 min. (*C*) Experimental height profile evolution of the PS droplet dewetting from DTS shown in *A*. Time between subsequent lines is ~4 min. (*Insets*) Height profiles, with the radial coordinate r and height profile $h(r,t)$ scaled by the contact line radius $R(t)$ and central droplet height $h(0,t)$. Inset color schemes as in the main figures.

the PS melt, and corrections of the normal stress by van der Waals forces are consistently neglected in the bulk equations. To account for slippage relative to the substrate, we impose a Navier slip condition, representing a balance of stresses parallel to the substrate. The radial velocity component u_r at the substrate then satisfies

$$\kappa u_r|_{z=0} = \eta \partial_z u_r|_{z=0}. \quad [1]$$

Eq. **1** allows for a definition of the slip length, $b = \eta/\kappa$, where κ is a constant friction coefficient. As a boundary condition on the height profile, we impose a microscopic contact angle equal to the final contact angle θ_∞ at the contact line position for all times (17, 18). This constant angle assumption is not strictly correct, yet, with the small variation observed in the experimental evolution, it is a reasonable approximation [examples for $\theta(t)$ are shown in Fig. S3]. In the following, we refer to this as the Navier–Young model (NYM). Given θ_0 and θ_∞ as control parameters, only two independent length scales can be found in the NYM for dewetting microdroplets. The droplet size represents the first length scale, e.g., R_0, whereas the second one is the Navier slip length b. Rescaling all lengths with R_0 and using a dimensionless time $\mathcal{T} \equiv \gamma t \eta^{-1} R_0^{-1}$, we end up with the three independent dimensionless control parameters: θ_0, θ_∞, and the rescaled slip length $\mathcal{B}$ defined above. The associated dimensionless contact line radius is $\mathcal{R}(\mathcal{T}) = R(t)/R_0$, with velocity $\dot{\mathcal{R}} = d\mathcal{R}/d\mathcal{T}$.

In Fig. 2 *A* and *B* we present temporal profile evolutions obtained from the NYM for $\mathcal{B} = 0.030$ and $\mathcal{B} = 0.47$. The droplets have geometrical and physical parameters that were chosen to match the experimental droplets shown in Fig. 1. Remarkably, these computed droplet evolutions reproduce the curvature inversion of Fig. 1*B* and its absence in Fig. 1*C*, confirming that slip plays a major role in determining the transient shape. In Fig. 2, we also add experimental data from Fig. 1 for the specific profiles that maximize the deviation from a spherical cap. Those experimental profiles show good quantitative agreement with the NYM profiles, with maximum relative deviations of $\sim 5\%$. Comparison with other experiments for different droplets, as well as for different times for the droplets presented in Fig. 2, shows similar agreement. We note that the deviation between experiments and the NYM is consistent with the typical experimental uncertainties, mainly comprising overshoot due to the large slopes encountered (55) (Fig. S4). Identifying the numerically computed shapes of Fig. 2*A* with the measured ones for the droplet on OTS of Fig. 1*B*, we note that $\mathcal{B} = 0.03$ corresponds to a slip length $b_{\mathrm{OTS}} = 160$ nm, which is exactly the value measured in the hole-growth dewetting experiment (51), as given above. For the droplet of Fig. 2*B*, $\mathcal{B} = 0.47$ corresponds to a slip length $b_{\mathrm{DTS}} = 2{,}250$ nm for the experimental droplet of Fig. 1*C*; this is similar to the measured slip length $b_{\mathrm{DTS}} = 1{,}500 \pm 200$ nm in ref. 51.

To understand the different shape evolutions in terms of the flow structure inside the droplets, we computed the flow fields from the NYM. The numerical solutions, superimposed on the 3D renderings shown in Fig. 2 *C* and *D*, reveal substantial qualitative differences in the spatial distribution of the flow inside the droplets at the early moment when $\mathcal{R} = 0.91$. As illustrated in Fig. 2*C*, the velocity field for small rescaled slip length $\mathcal{B} = 0.03$ is concentrated near the contact line and contains mainly shear flow. The result is an upward motion of the interface near the contact line but not in the central part of the drop. The formation of a ridge is thus observed later. In contrast to the droplet in Fig. 2 *A* and *C*, the flow field for a larger rescaled slip length $\mathcal{B} = 0.47$ in Fig. 2*D* is more delocalized, including a significant upward flow in the central part of the droplet. We note the disparity in arrow lengths and gray scale near the droplet centers in Fig. 2 *C* and *D*. The velocity field of Fig. 2*D* corresponds more to elongational flow throughout the droplet, with the flow profile close to the contact line more resembling a plug flow (i.e., constant radial velocity with respect to the vertical direction). These

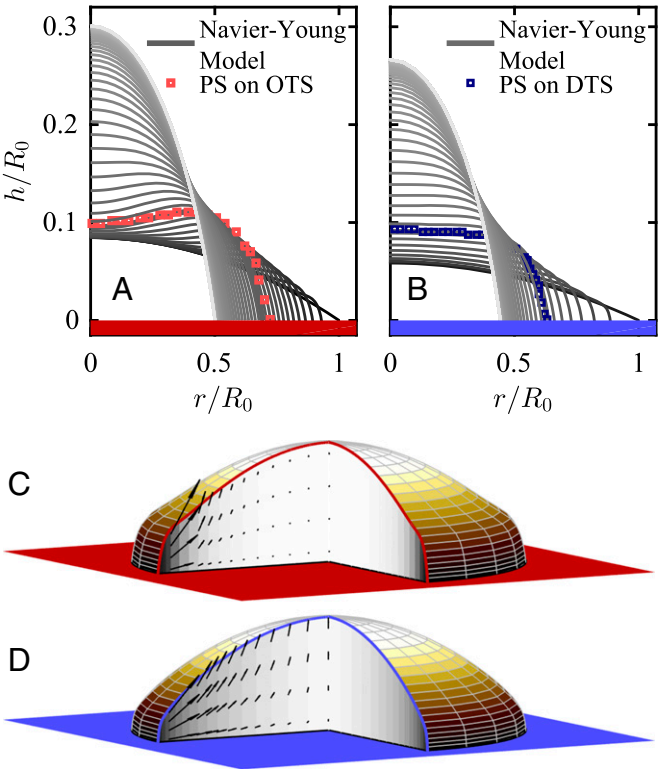

Fig. 2. (*A* and *B*) Normalized height profiles as a function of normalized radius, at different dimensionless times, $\mathcal{T}$, for numerical droplet evolutions obtained from the NYM: (*A*) $0 \le \mathcal{T} \le 14.5$, rescaled slip length $\mathcal{B} = 0.030$, $\theta_0 = 11°$, and $\theta_\infty = 62°$, as for the PS droplet evolution on OTS in Fig. 1*B*; (*B*) $0 \le \mathcal{T} \le 5.2$, $\mathcal{B} = 0.47$, $\theta_0 = 7.0°$, and $\theta_\infty = 62°$, as for the PS droplet on DTS in Fig. 1*C*. For both *A* and *B* experimental data from the highlighted transient profiles (gray lines of Fig. 1) are shown as squares. (*C* and *D*) Three-dimensional renderings of the droplet surfaces (note exaggerated vertical scales) with the flow fields when $\mathcal{R} = 0.91$ for the droplets shown in *A* and *B*. Gray scales indicate magnitudes of the dimensionless flow velocity for various r/R_0, averaged through the local interface height. Arrow lengths and gray scales are normalized by the respective contact line speeds, $|\dot{\mathcal{R}}| = 0.16$ and 1.19 for *C* and *D*.

differences between the two early flow fields are responsible for the transient ridge formation of the $\mathcal{B} = 0.03$ droplet and its absence for $\mathcal{B} = 0.47$.

Slip not only changes the structure of the flow field in the droplet, thus controlling the morphological evolution of the free interface during dewetting, but the magnitude of slip also has a significant impact on the rate of dewetting. The capillary numbers, $\mathrm{Ca} \equiv \dot{R}\eta/\gamma = \dot{\mathcal{R}}$, of the early flows are of order ~ 1 for DTS, and ~ 0.1 for OTS, which are much larger than those typically encountered in no-slip systems (16, 17, 27, 32, 33). To quantify the impact of slip on the dewetting dynamics, we consider the motion of the contact line. For ease of comparison, we normalize the displacement of the contact line, $R_0 - R(t)$, by the total change throughout the droplet equilibration, $R_0 - R_\infty$, where R_∞ is the asymptotically reached contact line radius in the equilibrium state. The evolution of the normalized contact line displacement as a function of time for the two droplets of Fig. 1 is shown in Fig. 3*A*; unscaled $R(t)$ are also shown in Fig. S1.

In both the OTS and DTS cases of Fig. 3, the contact line displacement during the earliest experimentally accessible time shows a power law $R_0 - R(t) \propto t^m$. In addition, we show in Fig. 3*A* (*Inset*) the measured exponents m of 10 other PS droplets as a function of $b\Omega^{-1/3}$, where Ω is the droplet volume. Remarkably, although the flow structure for different cases can be significantly

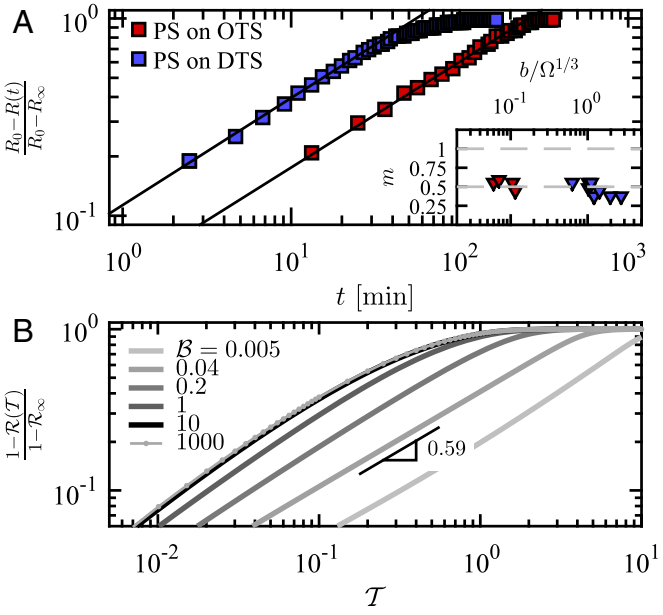

Fig. 3. (*A*) Experimental early-time dynamics of the normalized contact line radius, for the two PS droplets of Fig. 1, dewetting from OTS and DTS substrates. Solid lines represent power laws $\sim t^m$, with exponent $m=0.54$. (*Inset*) Such exponents measured for all studied droplets for which an early-time dynamics was accessible, as a function of $b\Omega^{-1/3}$, where Ω is the droplet volume; the dashed lines indicate $m=0.5$ and $m=1$. (*B*) Numerical early-time dynamics obtained from the NYM using various $\mathcal{B}=b/R_0$. Along with unit initial radius, parameters used were $\theta_0=9.9°$, $\theta_\infty=62°$, leading to $\mathcal{R}_\infty=R_\infty/R_0\approx 0.54$.

different, the observed value of m is well represented by the average on all droplets $\langle m\rangle=0.48\pm0.08$, with the error representing the SD. A power-law scaling of the contact line displacement in time similar to the experiments is obtained from the NYM (Fig. 3*B*) for rescaled slip length $0.03\lesssim\mathcal{B}\lesssim 1$, corresponding to the experimental range of $\mathcal{B}$. Deviations from an ideal power law become clearly visible for $\mathcal{B}=0.005$ and $\mathcal{B}\geq 10$.

In the numerical results of the NYM for both droplets represented in Fig. 2, we observe that the early-time frictional dissipation is concentrated near the contact line (Fig. S5). At early times, we thus assume the capillary driving power to be significantly dissipated by friction in the contact line region. Because the spreading parameter (14) reads $S=\gamma(\cos\theta_\infty-1)$, the typical driving power is $\sim SR_0\dot{R}\sim-\gamma R_0\dot{R}$. On the other hand, because the frictional stress scales as $\sim\kappa\dot{R}$, the frictional dissipation power is $\sim\eta\dot{R}^2R_0\Delta/b$ (see Eq. **1**), where $\Delta(t)$ is the typical horizontal extension of the flow region where friction is important. Supported by an argument based on a thin-film approximation of the flow and by the experimentally measured profiles near the contact line (*Supporting Information* and Fig. S6), we impose a proportionality between the vertical and horizontal extents of the slip region. Conservation of volume thus implies a scaling $R_0\Delta^2\sim R_0(R_0-R)^2$. Balancing the capillary driving power and the frictional dissipation power (56) thus leads to $\dot{R}(R-R_0)\sim\gamma b/\eta$, which can be integrated into

$$R_0-R(t)\sim\left(\frac{\gamma bt}{\eta}\right)^{1/2}, \qquad [2]$$

consistent with the values of m reported above in both experiments and numerics.

The scaling argument provided above assumes that friction at the substrate is a dominant dissipation mechanism, in addition to viscous processes (29). Using the NYM, we determine that friction at the substrate accounts for $\sim 60\%$ of the overall energy dissipation for $\mathcal{B}=0.03$ (OTS), and $\sim 40\%$ for $\mathcal{B}=0.47$ (DTS) during the early-time regime. Although these are not necessarily dominating, it is clear that frictional dissipation is largest near the contact line where friction dominates over viscous dissipation (Fig. S5). In contrast to the slip friction dominated scaling derived above, no-slip hole-growth dewetting is known to show a linear power law in time (45) (with logarithmic corrections). Similarly, following the arguments preceding Eq. **2** but with the friction replaced by viscous shear dissipation and adding a regularization mechanism appropriate to the no-slip situation, a linear power law $R_0-R(t)\sim t$ would be obtained. This shear dissipation dominated scaling prediction falls well outside our experimentally observed range of exponents in Fig. 3*A* (*Inset*), suggesting that dissipation in the contact line region is dominated by friction at early times.

For late-time dynamics of dewetting microdroplets, the precise value of the rescaled slip length $\mathcal{B}$ is also of great importance. In Fig. 4 *A* and *B*, we show the displacement $R(t)-R_\infty$ of the contact line with respect to the final contact line radius R_∞. As expected from a linear response, the contact line radius $R(t)$ saturates exponentially to the final equilibrium value R_∞. The same features

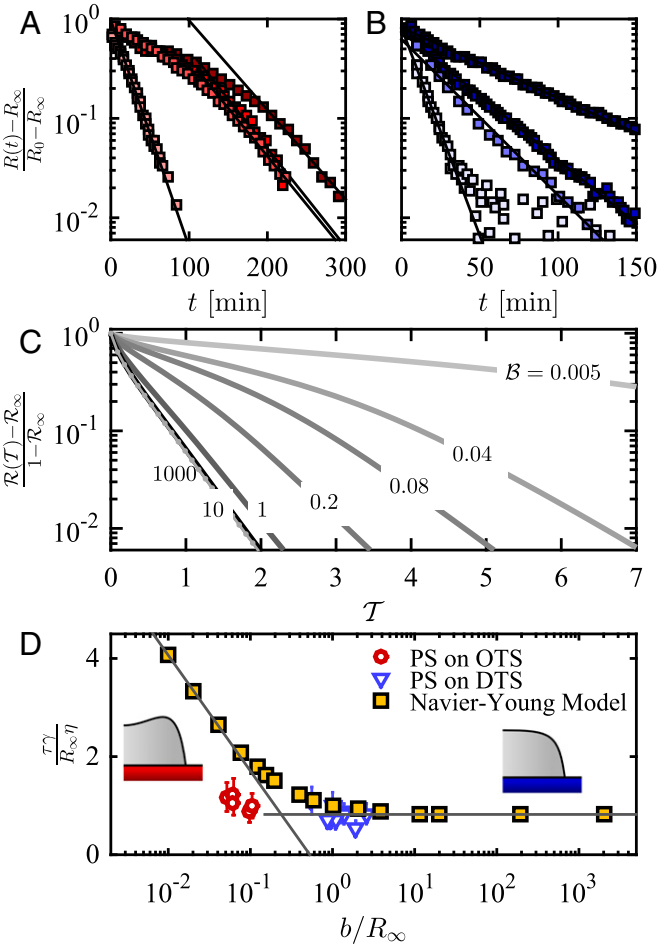

Fig. 4. Late-time dynamics of normalized contact line radius for (*A*) PS droplets dewetting from OTS covered substrates, with 2.7 μm $\leq R_0\leq$ 5.3 μm; (*B*) PS droplets dewetting from DTS covered substrates, with 1.8 μm $\leq R_0\leq$ 7.7 μm; (*C*) numerical results from the NYM, with dimensionless slip lengths $\mathcal{B}$ as indicated on the curves. (*D*) Dimensionless relaxation time constant as a function of dimensionless slip length, for both the experiments and the NYM. The two lines depict the asymptotic behaviors (see text following Eqs. **3** and **4**): (*i*) weak-slip logarithmic behavior; (*ii*) strong-slip constant behavior. (*Insets*) These recall intermediate-time droplet shapes, for the weak-slip (red substrate) and strong-slip (blue substrate) regimes.

are also clearly visible in the numerical solutions shown in Fig. 4*C* for various $\mathcal{B}$. Furthermore, on DTS, for the smallest droplets on OTS, and at large $\mathcal{B}$ in the NYM, the droplets reach this late-time regime at much larger $R-R_\infty$. Interestingly, an exponential relaxation to a spherical shape is also characteristic of suspended viscous droplets (57, 58). Thus, a connection can be drawn between supported droplets with large slip lengths and free-standing droplets. In fact, by symmetry, the freely relaxing droplets are strictly equivalent to infinite-slip dewetting droplets when $\theta_\infty = 90°$.

As for the early-time power law, the late-time exponential evolution can be understood from an energy balance. Close to equilibrium, the droplet shape is nearly a spherical cap, and the restoring capillary force is linear in $R-R_\infty$ (Eq. **S20**). The driving capillary power then scales as $\mathcal{P}_{\text{inj}} \sim -\gamma(R-R_\infty)\dot{R}$. On the other hand, the dissipation power $\mathcal{P}_{\text{dis}}$ depends on the four parameters, η, b, θ_∞, and R_∞ and the one variable, $\dot{R}$. By dimensional analysis (59), we can therefore write the dissipation power in the form $\mathcal{P}_{\text{dis}} \sim \eta R_\infty \dot{R}^2$, with a dimensionless prefactor that is a function of b/R_∞ and θ_∞ (recall that the latter is constant in this study). Equating the dissipation power with the driving one and integrating in time leads to

$$R(t) - R_\infty \sim \mathrm{e}^{-t/\tau}, \qquad [3]$$

$$\tau = \frac{\eta R_\infty}{\gamma} f\left(\frac{b}{R_\infty}, \theta_\infty\right), \qquad [4]$$

where f absorbs the numerical prefactors missing in the scaling arguments presented above. Fig. 4*D* displays the experimentally measured time constants, after a rescaling according to Eq. **4**, as a function of the dimensionless slip length b/R_∞ using $b_{\text{OTS}} = 160$ nm and $b_{\text{DTS}} = 2{,}250$ nm (Fig. 2). Numerically computed time constants from the NYM allow an estimate of the scaling function f in Eq. **4**, which is logarithmically decreasing for small b/R_∞ but tends to a constant value for large b/R_∞. Both asymptotic limits of the scaling function f can be understood from the viscous dissipation in the bulk flow during the late-time relaxation.

When $b/R_\infty \ll 1$, the dynamics can be analyzed in the framework of the classical wedge calculation (13, 16), where the slip length replaces the microscopic cutoff length scale in the logarithmic prefactor as discussed in the Introduction. In this limit, it follows for a spherical cap: $f = C_0 \ln(b/R_\infty) + C_1$, where $C_0 \approx -1.44$ for $\theta_\infty = 62°$ (*Supporting Information*). In Fig. 4*D*, we obtain $C_0^{\text{NYM}} = -1.02$ and $C_1^{\text{NYM}} = -0.65$ by fitting the $\mathcal{B} \le 0.08$ NYM data. Although the experimental data deviate slightly (*Supporting Information*), the numerical results are in reasonable agreement with the analytical calculation above.

In contrast to weak slip, when $b/R_\infty \gg 1$ the assumption of a localized dissipation near the contact line, inherent to the classical wedge calculation, is violated. Friction at the substrate is negligible with respect to elongational viscous stresses, and a different retraction regime is entered. In this regime, we expect f to be independent of b/R_∞. We find $f|_{b\to\infty} \approx 0.82$ for $\theta_\infty = 62°$ in the NYM; the experiments on DTS support this finding. The NYM value for the strong-slip relaxation time compares well with an estimate assuming viscous dissipation to occur only through elongational stresses. This simple model (*Supporting Information*) predicts $f|_{b\to\infty} \approx 1.05$ for $\theta_\infty = 62°$.

To conclude, we have studied polymer microdroplets dewetting from substrates decorated with SAMs. The OTS SAM provides a weaker slip boundary condition compared with the DTS one, resulting in marked differences in the evolution of similarly sized droplets. Specifically, the weaker slip condition can give rise to a transient ridge. Increasing the ratio of slip length to droplet size, we observe a gradual disappearing of the ridge. These observations are explained through visualizations of the flow fields accessed through the NYM. At early times, we find that the dewetting dynamics is in agreement with a scaling argument predicting a temporal power-law evolution of the dewetted distance, with an exponent 1/2, consistent with the NYM. At late times, an exponential saturation of the contact line radius with time is observed. The time constants are in good agreement with the scaling analysis and numerical solution of the NYM. This simple system of dewetting microdroplets on different surfaces gives insights on the effects of slip in free-surface micro- and nanoflows. In the context of the Huh–Scriven paradox of contact line motion, our work offers a combined experimental and theoretical justification for slip as a major control factor in the motion of contact lines.

Materials and Methods

To prepare the nonequilibrium droplets, PS (Polymer Standards Service GmbH) with weight-averaged molecular weight 10.3 kg/mol and polydispersity index 1.03, was dissolved into toluene (chromatography grade, Merck), and spin-coated onto freshly cleaved mica sheets (grade V2, Plano GmbH). After a dewetting process in toluene-saturated atmosphere at room temperature, glassy spherical cap-shaped droplets on mica were produced with initial contact angles $\theta_0 = 9 \pm 3°$, and contact line radii $2\ \mu\text{m} \lesssim R_0 \lesssim 7\ \mu\text{m}$ (measured using AFM; Dimension FastScan and FastScan A tips, Bruker).

Under ambient conditions, the glassy droplets were then floated from mica onto the surface of an ultraclean water bath (18 MΩ cm, total organic carbon content <6 ppb; TKA-GenPure, TKA Wasseraufbereitungssysteme GmbH), and transferred onto the SAM-coated silicon wafers [(100) crystal orientation with native oxide layer present; Si-Mat Silicon Materials]. Two types of SAMs were used, being prepared from either OTS or DTS; Sigma-Aldrich), with the self-assembly procedure and full characterization described in ref. 60. Both SAM coatings render the Si wafers hydrophobic, and lead to equilibrium PS contact angles in air of $\theta_\infty = 62 \pm 3°$, as measured by AFM.

The droplets dewet when heated above the glass-transition temperature ≈90 °C (61). The heating stage on the AFM was set to 110 °C and AFM was used to measure in situ height profiles of the dewetting microdroplets. This annealing temperature is low enough to ensure no loss of PS due to evaporation or degradation; volume conservation was verified. Finally, the capillary velocity of our system was measured using the stepped-film method (62) to be $\gamma/\eta = 0.07 \pm 0.01\ \mu\text{m min}^{-1}$ at the experimental annealing temperature.

ACKNOWLEDGMENTS. The authors gratefully acknowledge Natural Sciences and Engineering Research Council of Canada (NSERC), the Alexander von Humboldt Foundation, the German Science Foundation, and Total - ESPCI ParisTech Chair for financial support. J.D.M. was supported by LabEX ENS-ICFP: ANR-10-LABX-0010/ANR-10-IDEX-0001-02 PSL.

1. Bocquet L, Charlaix E (2010) Nanofluidics, from bulk to interfaces. *Chem Soc Rev* 39(3): 1073–1095.
2. Neto C, Evans D, Bonaccurso E, Butt HJ, Craig V (2005) Boundary slip in Newtonian liquids: A review of experimental studies. *Rep Prog Phys* 68(12):2859–2897.
3. Lauga E, Brenner M, Stone H (2007) *Handbook of Experimental Fluid Mechanics*, eds Tropea C, Yarin A, Foss J (Springer, New York).
4. Falk K, Sedlmeier F, Joly L, Netz RR, Bocquet L (2010) Molecular origin of fast water transport in carbon nanotube membranes: Superlubricity versus curvature dependent friction. *Nano Lett* 10(10):4067–4073.
5. Whitby M, Cagnon L, Thanou M, Quirke N (2008) Enhanced fluid flow through nanoscale carbon pipes. *Nano Lett* 8(9):2632–2637.
6. Cuenca A, Bodiguel H (2013) Submicron flow of polymer solutions: Slippage reduction due to confinement. *Phys Rev Lett* 110(10):108304.
7. Setu SA, et al. (2015) Superconfinement tailors fluid flow at microscales. *Nat Commun* 6:7297, 10.1038/ncomms8297.
8. Bäumchen O, et al. (2014) Influence of slip on the Rayleigh-Plateau rim instability in dewetting viscous films. *Phys Rev Lett* 113(1):014501.
9. Bäumchen O, Fetzer R, Jacobs K (2009) Reduced interfacial entanglement density affects the boundary conditions of polymer flow. *Phys Rev Lett* 103(24):247801.
10. Haefner S, et al. (2015) Influence of slip on the Plateau-Rayleigh instability on a fibre. *Nat Commun* 6:7409.
11. Huh C, Scriven L (1971) Hydrodynamic model of steady movement of a solid/liquid/fluid contact line. *J Colloid Interface Sci* 35(1):85–101.
12. Dussan VE, Davis S (1974) On the motion of a fluid-fluid interface along a solid surface. *J Fluid Mech* 65(01):71–95.
13. de Gennes P (1985) Wetting: Statics and dynamics. *Rev Mod Phys* 57:827–863.
14. de Gennes P, Brochard-Wyart F, Quéré D (2003) *Capillarity and Wetting Phenomena: Drops, Bubbles, Pearls, Waves* (Springer, New York).
15. Blake TD (2006) The physics of moving wetting lines. *J Colloid Interface Sci* 299(1): 1–13.

16. Bonn D, Eggers J, Indekeu J, Meunier J, Rolley E (2009) Wetting and spreading. *Rev Mod Phys* 81(2):739–805.
17. Snoeijer J, Andreotti B (2013) Moving contact lines: Scales, regimes, and dynamical transitions. *Annu Rev Fluid Mech* 45:269–292.
18. Sibley D, Nold A, Savva N, Kalliadasis S (2014) A comparison of slip, disjoining pressure, and interface formation models for contact line motion through asymptotic analysis of thin two-dimensional droplet spreading. *J Eng Math*, 10.1007/s10665-014-9702-9.
19. Heslot F, Cazabat A, Fraysse N (1989) Diffusion-controlled wetting films. *J Phys Condens Matter* 1(33):5793–5798.
20. Cazabat A, Gerdes S, Valignat M, Vilette S (1997) Dynamics of wetting: From theory to experiment. *Interface Sci* 5(2):129–139.
21. Kavehpour HP, Ovryn B, McKinley GH (2003) Microscopic and macroscopic structure of the precursor layer in spreading viscous drops. *Phys Rev Lett* 91(19):196104.
22. Ghosh M, Stebe KJ (2010) Spreading and retraction as a function of drop size. *Adv Colloid Interface Sci* 161(1-2):61–76.
23. Hoang A, Kavehpour HP (2011) Dynamics of nanoscale precursor film near a moving contact line of spreading drops. *Phys Rev Lett* 106(25):254501.
24. Cormier SL, McGraw JD, Salez T, Raphaël E, Dalnoki-Veress K (2012) Beyond Tanner's law: Crossover between spreading regimes of a viscous droplet on an identical film. *Phys Rev Lett* 109(15):154501.
25. Cantat I (2014) Liquid meniscus friction on a wet plate: Bubbles, lamellae, and foams. *Phys Fluids* 25(3):031303.
26. Wayner P (1993) Spreading of a liquid film with a finite contact angle by the evaporation/condensation process. *Langmuir* 9(1):294–299.
27. Davitt K, Pettersen MS, Rolley E (2013) Thermally activated wetting dynamics in the presence of surface roughness. *Langmuir* 29(23):6884–6894.
28. Thompson PA, Troian SM (1997) A general boundary condition for liquid flow at solid surfaces. *Nature* 389:360–362.
29. van Lengerich HB, Steen PH (2012) Energy dissipation and the contact-line region of a spreading bridge. *J Fluid Mech* 703(7):111–141.
30. Kirkinis E, Davis SH (2013) Hydrodynamic theory of liquid slippage on a solid substrate near a moving contact line. *Phys Rev Lett* 110(23):234503.
31. Weiqing R, Weinan E (2007) Boundary conditions for the moving contact line problem. *Phys Fluids* 19(2):022101.
32. Marsh JA, Garoff S, Dussan V (1993) Dynamic contact angles and hydrodynamics near a moving contact line. *Phys Rev Lett* 70(18):2778–2781.
33. Delon G, Fermigier M, Snoeijer JH, Andreotti B (2008) Relaxation of a dewetting contact line part 2: Experiments. *J Fluid Mech* 604(6):55–75.
34. Eggers J (2005) Existence of receding and advancing contact lines. *Phys Fluids* 17(8): 082106.
35. Chan T, Gueudré T, Snoeijer J (2011) Maximum speed of dewetting on a fiber. *Phys Fluids* 23(11):112103.
36. Navier C (1823) Mémoire sur les lois du mouvement des fluides. *Mem Acad Sci Inst Fr* 6:389–416.
37. Cho JHJ, Law BM, Rieutord F (2004) Dipole-dependent slip of Newtonian liquids at smooth solid hydrophobic surfaces. *Phys Rev Lett* 92(16):166102.
38. Joly L, Ybert C, Bocquet L (2006) Probing the nanohydrodynamics at liquid-solid interfaces using thermal motion. *Phys Rev Lett* 96(4):046101.
39. Cottin-Bizonne C, Steinberger A, Cross B, Raccurt O, Charlaix E (2008) Nanohydrodynamics: The intrinsic flow boundary condition on smooth surfaces. *Langmuir* 24(4):1165–1172.
40. Guriyanova S, Semin B, Rodrigues TS, Butt HJ, Bonaccurso E (2010) Hydrodynamic drainage force in a highly confined geometry: Role of surface roughness on different length scales. *Microfluid Nanofluidics* 8(5):653.
41. Pit R, Hervet H, Léger L (2000) Direct experimental evidence of slip in hexadecane: solid interfaces. *Phys Rev Lett* 85(5):980–983.
42. Schmatko T, Hervet H, Léger L (2005) Friction and slip at simple fluid-solid interfaces: The roles of the molecular shape and the solid-liquid interaction. *Phys Rev Lett* 94(24): 244501.
43. Leroy S, Restagno F, Charlaix E (2009) Fine calibration of the residual dissipation in a surface forces apparatus using a capacitive sensor. *Rev Sci Instrum* 80(8):653–663.
44. de Gennes P (1997) *Soft Interfaces: The 1994 Dirac Memorial Lecture* (Cambridge Univ Press, Cambridge, UK).
45. Brochard-Wyart F, de Gennes P, Hervet H, Redon C (1994) Wetting and slippage of polymer melts on semi-ideal surfaces. *Langmuir* 10(5):1566–1572.
46. Maxwell B, Galt JC (1962) Velocity profiles for polyethyene melt in tubes. *Journal of Polymer Science* 62(174):S50–S53.
47. Reiter G, Khanna R (2000) Kinetics of autophobic dewetting of polymer films. *Langmuir* 16(15):6351–6357.
48. Léger L (2003) Friction mechanisms and interfacial slip at fluid–solid interfaces. *J Phys Condens Matter* 15(1):S19–S29.
49. Fetzer R, Jacobs K, Münch A, Wagner B, Witelski TP (2005) New slip regimes and the shape of dewetting thin liquid films. *Phys Rev Lett* 95(12):127801.
50. Fetzer R, Münch A, Wagner B, Rauscher M, Jacobs K (2007) Quantifying hydrodynamic slip: A comprehensive analysis of dewetting profiles. *Langmuir* 23(21):10559–10566.
51. McGraw JD, et al. (2014) Nanofluidics of thin polymer films: Linking the slip boundary condition at solid-liquid interfaces to macroscopic pattern formation and microscopic interfacial properties. *Adv Colloid Interface Sci* 210:13–20.
52. Gutfreund P, et al. (2013) Solid surface structure affects liquid order at the polystyrene-self-assembled-monolayer interface. *Phys Rev E Stat Nonlin Soft Matter Phys* 87(1):012306.
53. Bäumchen O, et al. (2012) Slippage and nanorheology of thin liquid polymer films. *J Phys Condens Matter* 24(32):325102, 1–17.
54. Pozrikidis C (2002) *A Practical Guide to Boundary Element Methods* (Chapman & Hall/CRC, Boca Raton, FL).
55. Chasiotis I (2008) Atomic force microscopy in solid mechanics. *Springer Handbook of Experimental Solid Mechanics*, ed Sharpe W (Springer, New York), pp 409–444.
56. Nakamura Y, Carlson A, Amberg G, Shiomi J (2013) Dynamic wetting at the nanoscale. *Phys Rev E Stat Nonlin Soft Matter Phys* 88(3):033010.
57. Rallison J (1984) The deformation of small viscous drops and bubbles in shear flows. *Annu Rev Fluid Mech* 16:45–66.
58. Guido S, Villone M (1999) Measurement of interfacial tension by drop retraction analysis. *J Colloid Interface Sci* 209(1):247–250.
59. Barenblatt G (2003) *Scaling* (Cambridge Univ Press, Cambridge, UK).
60. Lessel M, et al. (2015) Self-assembled silane monolayers: An efficient step-by-step recipe for high-quality, low energy surfaces. *Surf Interface Anal* 47(5):557–564.
61. Santangelo P, Roland C (1998) Molecular weight dependence of fragility in polystyrene. *Macromolecules* 31(14):4581–4585.
62. McGraw JD, Salez T, Bäumchen O, Raphaël E, Dalnoki-Veress K (2012) Self-similarity and energy dissipation in stepped polymer films. *Phys Rev Lett* 109(12):128303.
63. Knoll A, Magerle R, Krausch G (2001) Tapping mode atomic force microscopy on polymers: Where is the true sample surface? *Macromolecules* 34(12):4159–4165.
64. Fetzer R, Rauscher M, Seemann R, Jacobs K, Mecke K (2007) Thermal noise influences fluid flow in thin films during spinodal dewetting. *Phys Rev Lett* 99(11):114503.
65. Münch A, Wagner B, Witelski T (2005) Lubrication models with small to large slip lengths. *J Eng Math* 53(3):359–383.

Supporting Information

McGraw et al. 10.1073/pnas.1513565113

Experimental Error and Model Deviations

We note that relative deviations between profiles predicted by the NYM and those measured with AFM are up to 5% (Fig. 2, main text). Because the typical contact angles are rather high, $\theta \approx 60°$, overshoot can affect the absolute height measurement in the forward and reverse directions. We show an example of this overshoot in Fig. S4, where the feedback parameters that control the interaction between the AFM tip and the substrate and droplet surfaces are tuned to minimize the difference between forward and reverse traces, while allowing for a minimum tip penetration (63). The typical deviations associated with various instrumental effects for the parameter settings of this scan (and those presented in the rest of the paper) are thus on the order of 1%. However, independent checks on static profiles have shown that the overshoot presented here is rate dependent, and can lead to variations on the height of 5%. Thus, the overall error on the height measurement at the ridge is roughly the same as the discrepancy between experiment and the NYM. Based on the profiles alone, a discrepancy between the NYM and the experiments cannot be resolved.

Although we cannot rule out other models that would change predicted profile shapes beyond the resolution of the current measurements (i.e., $\sim$ 5% relative error), our numerical model with Navier slip and Young-angle boundary condition has quantitatively corroborated the experimental height profile evolutions. Furthermore, the NYM and the scaling approaches have captured the main features of the contact line dynamics. However, we caution that the agreement is not quantitative in all respects. At small b/R_∞, the experimental time constants in Fig. 4*D* deviate from the NYM data and the scaling asymptotics. Several effects may explain this discrepancy: nonlinear (28) or spatially nonuniform (29, 30) slip may be operative; the assumption of constant microscopic contact angle (17, 18), $\theta(t) = \theta_\infty$, could be relaxed as well (Fig. S3); furthermore, in ultrathin ($\sim$5 nm) dewetting polymer films, thermal fluctuations are known to enhance the dynamics (64), which could also affect the effective liquid mobility at the solid–liquid boundary, or at the three-phase contact line. Additionally, at relatively small slip length, other mechanisms of CLM may contribute (16). The present results thus open a perspective to more detailed studies from both theoretical and experimental sides.

Asymptotic Early-Time Scaling

Here, we provide quantitative arguments for the scaling law given in Eq. **2**, using lubrication theory. Because the experiments are performed in a situation where the slip length b is comparable to the initial droplet radius R_0, and because we focus on the short-term asymptotic behavior near the contact line, we invoke the 2D thin-film equation for intermediate slip (65):

$$\partial_t h + \frac{\gamma b}{\eta}\,\partial_x\left(h^2\partial_x^3 h\right) = 0, \qquad \textbf{[S1]}$$

where γ is the PS–air surface tension and η the PS shear viscosity. This partial differential equation describes the viscocapillary evolution of a thin liquid film of profile $h(x,t)$ in space x (coordinate taken in the frame of the substrate) and time t, with intermediate slip at the substrate. The contact line is located at $x = R(t)$, and the liquid film is chosen to occupy the $x < R(t)$ region. The two boundary conditions at the contact line are thus $h(R(t),t) = 0$ and $\partial_x h(R(t),t) = -\tan\theta_\infty$. We thus assume an equilibrium microscopic contact angle θ_∞ at any time, consistent with the NYM used in the numerics. Let us nondimensionalize the problem through $x = XR_0$, $t = T\eta R_0^2/\gamma b$, $R(t) = \mathcal{R}(T)R_0$, $h(x,t) = H(X,T)R_0$, such that

$$\partial_T H + \partial_X\left(H^2\partial_X^3 H\right) = 0. \qquad \textbf{[S2]}$$

We now look for a self-similar asymptotic form at short times near the contact line:

$$H(X,T) = T^\alpha F\left(\widetilde{U}\right), \qquad \textbf{[S3]}$$

$$\widetilde{U} = \frac{X - \mathcal{R}(T)}{T^\beta}, \qquad \textbf{[S4]}$$

where α and β are unknown exponents, and $\mathcal{R}(T)$ is the law of interest. Invoking the boundary conditions above, one obtains $\alpha = \beta$, $F(0) = 0$, and $F'(0) = -\tan\theta_\infty$. Then, injecting the self-similar form into Eq. **S2**, one gets

$$\alpha\left(F - \widetilde{U}F'\right) = \dot{\mathcal{R}}T^{1-\alpha}F' - T^{1-2\alpha}\left(F^2F'''\right)', \qquad \textbf{[S5]}$$

where the prime represents the derivative with respect to $\widetilde{U}$, and the dot represents the derivative with respect to T. The proposed self-similar form is a possible solution if and only if the previous equation is an ordinary differential equation (ODE) on the single variable $\widetilde{U}$. One possibility is thus given by $\alpha = 1/2$, together with

$$\mathcal{R} = 1 - C\sqrt{T}, \qquad \textbf{[S6]}$$

which satisfies the initial condition, where C is a positive numerical constant, and where the minus sign corresponds to the dewetting situation. In that case, the ODE satisfied by F reads

$$F + \left(C - \widetilde{U}\right)F' + 2\left(F^2F'''\right)' = 0. \qquad \textbf{[S7]}$$

The latter could be solved numerically by adding three boundary conditions—especially in the unperturbed far-field region—and by shooting on C. Finally, putting back real dimensions, one obtains

$$R_0 - R(t) = C\sqrt{\frac{\gamma b t}{\eta}}, \qquad \textbf{[S8]}$$

which demonstrates the scaling law of Eq. **2** in the main text. Furthermore, one can validate the proposed self-similar form by comparison with the experimental profiles, as shown in Fig. S6.

We note that the essential ingredients in both the power balance and the thin-film equation are the same: capillarity drives a viscous flow and the dissipation is mostly due to friction at the substrate. The fact that we neglected the H^3 term in the thin-film equation, according to the intermediate-slip model (65), is consistent with the fact that we also neglected the bulk viscous dissipation near the contact line in the power balance leading to the scaling of Eq. **2**.

Asymptotic Late-Time Scalings

We will assume that the shape of the contracting droplet is close to that of a spherical cap. In the late-time regime of the contraction process, the apparent contact angle θ (evaluated through the assumed spherical cap profile) deviates from the microscopic contact angle θ_∞, but the difference $\theta - \theta_\infty$ is small and approaches nil at asymptotically large times.

The interfacial energy of a spherical cap with an apparent contact angle θ is given by

$$E=\gamma(A_{\rm lv}-\cos\theta_\infty A_{\rm sl}), \qquad \textbf{[S9]}$$

where we have defined the area of the substrate wet by liquid,

$$A_{\rm sl}=\pi R^2, \qquad \textbf{[S10]}$$

and the interfacial area between the liquid spherical cap and the vapor phase,

$$A_{\rm lv}=\frac{2\pi(1-\cos\theta)R^2}{\sin^2\theta}. \qquad \textbf{[S11]}$$

The contact line radius R is linked to the apparent contact angle θ by the condition that the volume of the liquid,

$$\Omega=\frac{\pi(1-\cos\theta)^2(2+\cos\theta)\,R^3}{3\sin^3\theta}, \qquad \textbf{[S12]}$$

is constant.

We first invert Eq. **S12** to obtain

$$R=\left[\frac{3\Omega\sin^3\theta}{\pi(1-\cos\theta)^2(2+\sin\theta)}\right]^{1/3}, \qquad \textbf{[S13]}$$

and insert the latter into Eqs. **S10** and **S11**. We thus obtain from Eq. **S9** the total interfacial energy of the spherical cap $E(\theta)$ as a function of the apparent contact angle θ only. We find

$$\left.\frac{{\rm d}E}{{\rm d}\theta}\right|_{\theta=\theta_\infty}=0, \qquad \textbf{[S14]}$$

as expected in mechanical equilibrium for $\theta=\theta_\infty$, and a second derivative

$$\left.\frac{{\rm d}^2E}{{\rm d}\theta^2}\right|_{\theta=\theta_\infty}=\frac{2\pi R_\infty^2}{2+\cos\theta_\infty}>0, \qquad \textbf{[S15]}$$

because the spherical cap is a stable shape.

Similarly, we could use an energy $\widetilde{E}(R)$ that depends only on the radius of the contact line R and $\theta(R)$. The results are

$$\left.\frac{{\rm d}\widetilde{E}}{{\rm d}R}\right|_{R=R_\infty}=0, \qquad \textbf{[S16]}$$

and

$$\left.\frac{{\rm d}^2\widetilde{E}}{{\rm d}R^2}\right|_{R=R_\infty}=2\pi(2+\cos\theta_\infty)\sin^2\theta_\infty>0. \qquad \textbf{[S17]}$$

Here, we make use of the chain rule of differentiation:

$$\left.\frac{{\rm d}\widetilde{E}}{{\rm d}R}\right|_{R=R_\infty}\equiv\left.\frac{{\rm d}E}{{\rm d}\theta}\right|_{\theta=\theta_\infty}\left.\left(\frac{{\rm d}R}{{\rm d}\theta}\right)^{-1}\right|_{\theta=\theta_\infty}, \qquad \textbf{[S18]}$$

and the identity

$$\left.\frac{{\rm d}^2\widetilde{E}}{{\rm d}R^2}\right|_{R=R_\infty}\equiv\left.\frac{{\rm d}^2E}{{\rm d}\theta^2}\right|_{\theta=\theta_\infty}\left.\left(\frac{{\rm d}R}{{\rm d}\theta}\right)^{-2}\right|_{\theta=\theta_\infty}, \qquad \textbf{[S19]}$$

which holds for an equilibrium state at $\theta=\theta_\infty$ and $R=R_\infty$.

Expanding the energy $\widetilde{E}(R)$ around $R=R_\infty$ up to second order yields

$$\widetilde{E}=\widetilde{E}_\infty+\pi\gamma(2+\cos\theta_\infty)\,\sin^2\theta_\infty\,(R-R_\infty)^2, \qquad \textbf{[S20]}$$

which, when differentiated with respect to $R-R_\infty$, yields a linear restoring force as claimed in the main text. The injected power from the gain of interfacial energy then reads

$$\mathcal{P}_{\rm inj}=2\pi\gamma(2+\cos\theta_\infty)\,\sin^2\theta_\infty\,(R-R_\infty)\,\dot{R}. \qquad \textbf{[S21]}$$

Weak Slip: $b\ll R$. In the limit of weak slip, the dissipation is mainly due to viscous losses in the bulk flow close to the contact line. In this contact line region, the free-surface profile of the droplet is assumed to be a wedge described by $z=h(x,t)=x\theta$, where x denotes the distance from the contact line. When the droplet spreads with a contact line velocity $\dot{R}$, there is a flow in the wedge that is described by a Poiseuille velocity profile:

$$v=\frac{3\dot{R}}{2h^2}\,z(z-2h), \qquad \textbf{[S22]}$$

with a local average velocity $(\int_0^h dz\ v)/h=\dot{R}$, and where we assumed a no-slip boundary condition at the substrate and a no-shear boundary condition at the free surface. The partial-slip boundary condition gives a noticeable departure from the Poiseuille profile only in the vicinity of the contact line where $h(x)\lesssim\theta\ell_{\rm m}$, with a microscopic length, $\ell_{\rm m}=\widetilde{C}\,b$, where $\widetilde{C}\sim\mathcal{O}(1)$. Therefore, the viscous dissipation power reads

$$\mathcal{P}_{\rm dis}=2\pi\eta R_\infty\int_{\ell_{\rm m}}^{R_\infty}dx\int_0^h dz\ (\partial_z v)^2=\frac{6\pi\eta R_\infty\dot{R}^2}{\theta_\infty}\ln\left(\frac{R_\infty}{\widetilde{C}\,b}\right). \qquad \textbf{[S23]}$$

Balancing the dissipated power, Eq. **S23**, and the injected power, Eq. **S21**, yields a differential equation for $R(t)$ with the solution

$$R(t)-R_\infty\sim\exp\left(-\frac{t}{\tau}\right), \qquad \textbf{[S24]}$$

with a time constant

$$\tau=\frac{\gamma R_\infty}{\eta}\,f(b/R_\infty), \qquad \textbf{[S25]}$$

$$f(b/R_\infty)=-\frac{3\ln(b/R_\infty)}{\theta_\infty(2+\cos\theta_\infty)\sin^2\theta_\infty}+C_1, \qquad \textbf{[S26]}$$

where C_1 is a nonuniversal constant that depends on the global interfacial geometry. Identifying Eq. **S26** with the corresponding expression in the main text, $f=C_0\ln(b/R_\infty)+C_1$, and substituting $\theta_\infty=62\,^\circ$, we find $C_0=1.44$.

Strong Slip: $b\gg R$. Because of incompressibility we have ${\rm Tr}(\dot{\boldsymbol{\epsilon}})=0$ for the rate-of-strain tensor $\dot{\boldsymbol{\epsilon}}$. For flat droplets $\theta_\infty\ll 1$, we can assume an axially symmetric and uniform straining flow in the horizontal and vertical direction of the droplet. In particular, we find that the rate of strain $\dot{\epsilon}_z$ into the axial direction is twice the rate of strain in the two directions parallel to the substrate:

$$\dot{\epsilon}_x=\dot{\epsilon}_y=-\frac{\dot{\epsilon}_z}{2}. \qquad \textbf{[S27]}$$

For a Newtonian fluid, we have $\boldsymbol{\sigma}=\eta\dot{\boldsymbol{\epsilon}}$, which provides us with the viscous dissipation:

$$\mathcal{P}_{\rm dis} = \int \mathrm{d}V\, \boldsymbol{\sigma} : \dot{\boldsymbol{\epsilon}}, \qquad \textbf{[S28]}$$

which yields

$$\mathcal{P}_{\rm dis} = 12\, \eta\, \dot{\epsilon}^2\, \Omega, \qquad \textbf{[S29]}$$

where the volume Ω is given by Eq. **S12**. Balancing the injected power of Eq. **S21** with the dissipated power of Eq. **S29**, and relations $\dot{R}/R = \dot{\epsilon}_x = \dot{\epsilon}_y$, we finally arrive at the relaxation timescale:

$$\tau(\theta_\infty) = \frac{\eta R_\infty}{\gamma} \frac{2(1-\cos\theta_\infty)^2}{\sin^5\theta_\infty}, \qquad \textbf{[S30]}$$

valid in the limit of full slip $b/R_\infty \to \infty$. For the particular case considered here, we have

$$\tau(62°) \approx 1.05\, \frac{\eta R_\infty}{\gamma}. \qquad \textbf{[S31]}$$

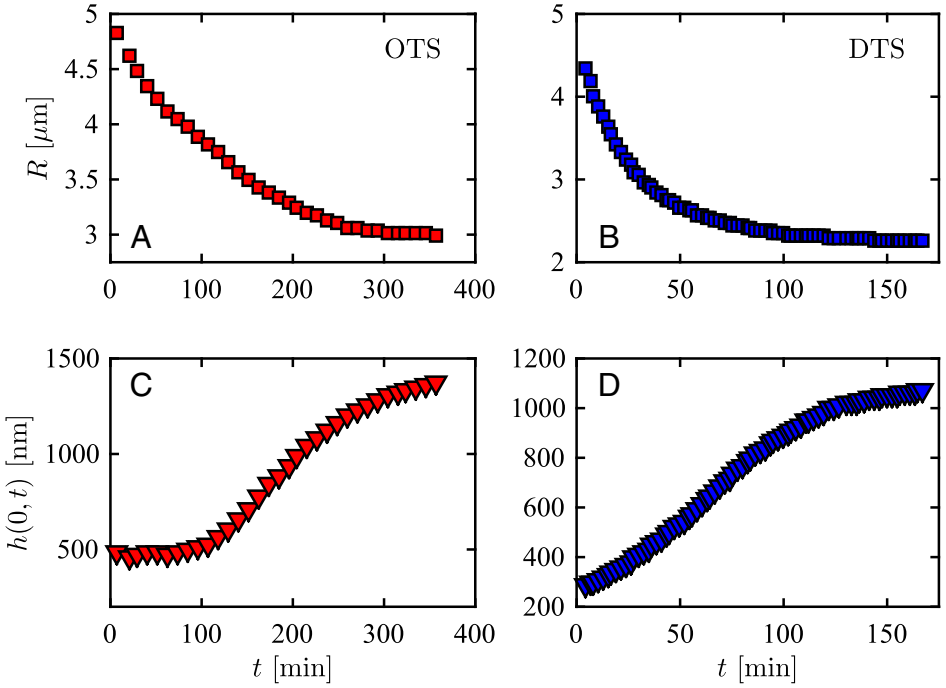

Fig. S1. Experimental contact line radius for the 10.3-kg/mol PS droplets dewetting from OTS (*A*) and DTS (*B*), as shown in Fig. 1 of the main text. (*C* and *D*) Central height evolutions for the same droplets. Note the approximately constant central height for the droplet on (*C*) OTS (smaller slip, see main text) at early times, compared with the central height for the droplet on (*D*) DTS (larger slip, see main text) whose height is increasing from the first experimentally accessible time.

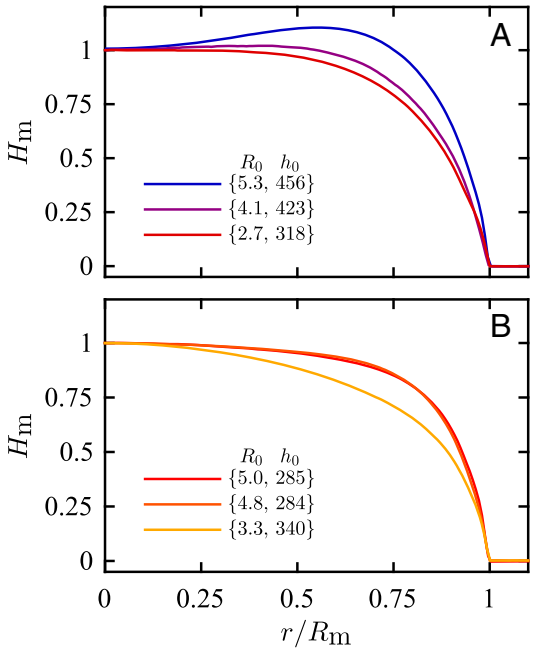

Fig. S2. (*A*) Experimental AFM data for PS microdroplets dewetting from OTS; here, $H_m(r/R_m) = h(r, t_m)/h(0, t_m)$, where the subscript "m" refers to the time when the height profile achieves maximal deviation from a spherical cap (compare gray lines in Fig. 1 of the main text). The legend shows the initial contact line radius, R_0 in micrometers and the initial central height, h_0, in nanometers. The ridge disappears for an initial contact line radius in the range 2.7 μm $< R_0 <$ 4.1 μm (slip length, $b_{OTS} \approx 160$ nm). (*B*) Conversely, the ridge does not appear for droplets with $R_0 \approx 5$ μm and below when dewetting from DTS ($b_{DTS} \approx 2{,}250$ nm), even while the initial contact angle, θ_0, is slightly smaller in the DTS case.

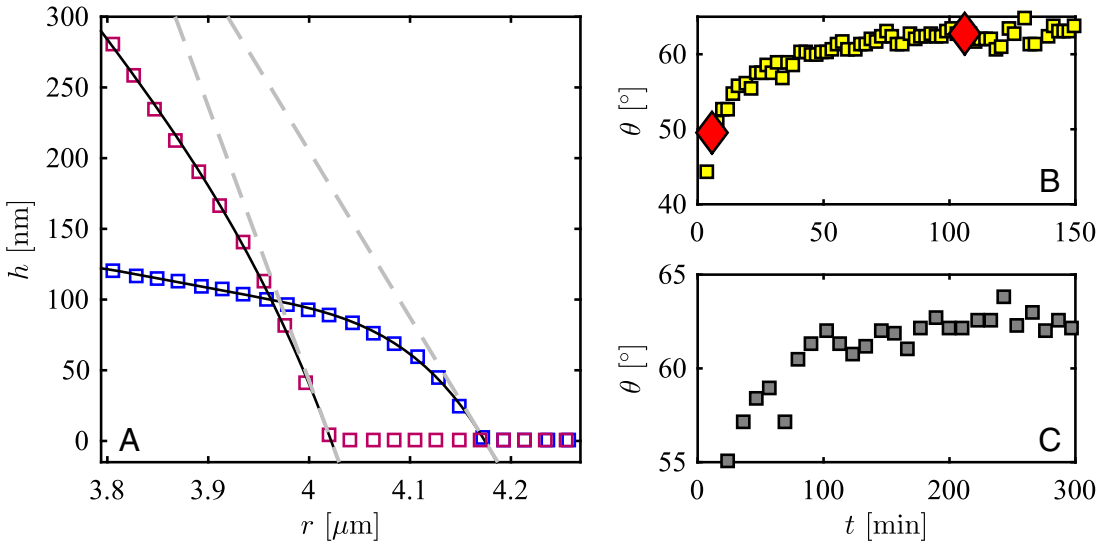

Fig. S3. (*A*) Experimental height profiles of a dewetting PS droplet on DTS (compare Fig. 1 of the main text), from which contact angles, $\theta(t)$, can be obtained. The tangents (dashed gray lines) of a fourth-order polynomial fit to the data (solid lines, not all fitted data shown) at the substrate, i.e., at $h = 0$, are obtained. The curve with larger contact angle has been shifted horizontally for clarity. (*B*) Contact angle as a function of time for the droplet represented in *A*. Red lozenges indicate the curves shown in *A*. We note that the initial angle (before dewetting starts) is $\theta_0 \approx 7°$. (*C*) Contact angle as a function of time for the PS droplet on OTS shown in Fig. 1 of the main text.

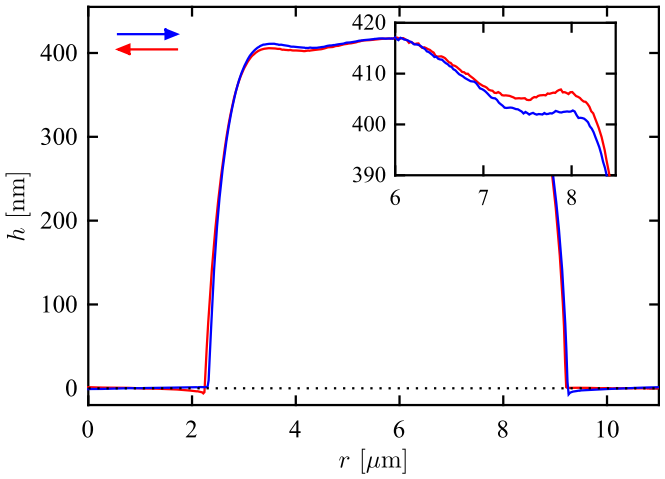

Fig. S4. Full height profiles for the forward (blue, left to right) and backward (red, right to left) traces of the AFM tip over a 10-kg/mol PS droplet dewetting from OTS at 110 ° C. Contact angles as shown in Fig. S3 are only measured in directions where there is no overshoot on the substrate.

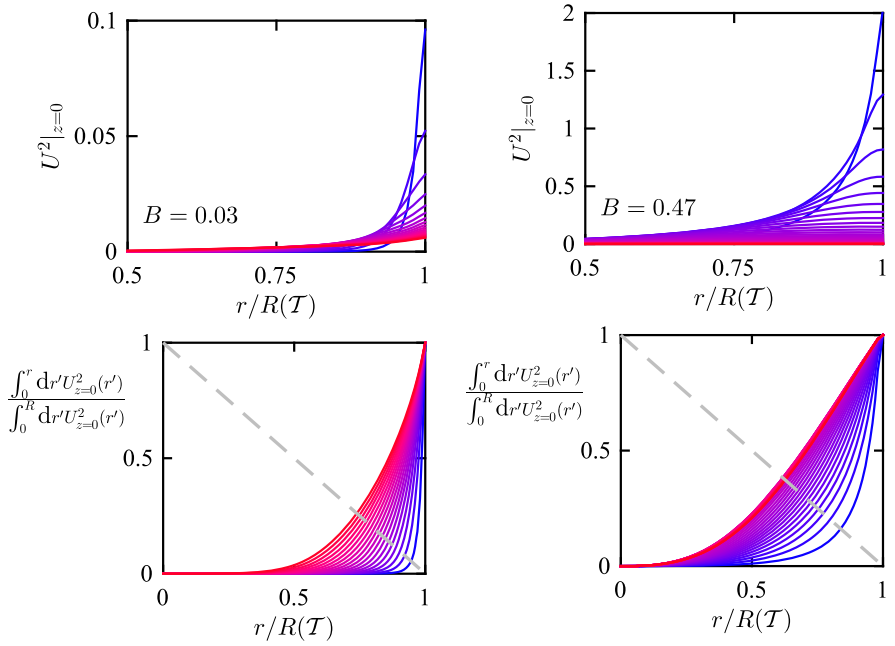

Fig. S5. (*Top*) Squared slip velocity (i.e., the fluid velocity at the substrate) as a function of the radial position, normalized by the contact line radius. The dimensionless slip lengths are the same as those for the droplets shown in Fig. 2 of the main text. (*Bottom*) Normalized frictional dissipation power (i.e., the dissipation due to fluid sliding against the solid substrate) on a disk of size r as a function of the normalized radial coordinate. The dashed line represents $y = 1 - x$ with y the vertical coordinate and x the horizontal one. The points at which the solid lines cross the dashed one are always below $y = 0.5$, which demonstrates that most of the frictional dissipation occurs near the contact line for both cases, especially at early times (blue).

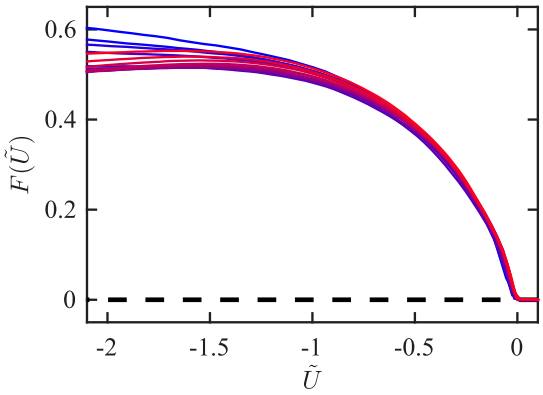

Fig. S6. Self-similar representation (Eqs. **S3** and **S4**) of early-time profiles for a 10-kg/mol PS droplet at 110 °C dewetting on a Si substrate coated with OTS, for times 20 min $< t <$ 160 min.